Nanoscale Advances

ROYAL SOCIETY OF CHEMISTRY

PAPER

View Article Online
View Journal | View Issue

Cite this: *Nanoscale Adv.*, 2025, **7**, 4673

A microelectromechanical system-based terahertz spiral metamaterial for pneumatic pressure sensing applications

Binghui Li[a] and Yu-Sheng Lin *[b]

Electromagnetic metamaterials have supported the realization of various highly effective sensors for chemical and biological detection. However, their application in pressure sensing has rarely been discussed. In this paper, we present a terahertz (THz) spiral metamaterial (TSM) integrated with microelectromechanical system (MEMS) technology for pneumatic pressure sensing applications. To improve the performance of the measuring range, the geometrical parameters of the TSM device are discussed, and the perfect absorption is achieved at 2.055 THz. Based on deformable construction, the TSM device can be designed for pneumatic pressure sensors, and the sensing performance is characterized by the relationship between resonant frequency and fluid pressure. The results show that the sensitivity of the TSM device to pressure force is 75 GHz kPa^{-1}. Meanwhile, the behavior of the TSM device exposed to an ambient environment with different refraction indices indicates its potential for biochemical sensing, and the sensitivity is up to 1.290 THz per RIU. These results offer a practical and compact multifunctional sensor for biochemical and pressure detection and open an avenue for applications in the field of THz optoelectronics.

Received 21st April 2025
Accepted 10th June 2025

DOI: 10.1039/d5na00384a

rsc.li/nanoscale-advances

1. Introduction

Metamaterials are artificially designed materials arranged by specifically engineered subwavelength unit cells. Through the enhancement of the interaction between electromagnetic waves and matter, metamaterials enable efficient manipulation of light.[1–3] There are many excellent phenomena that have been derived, including negative refractive indices,[4–6] surface enhancement,[7,8] chirality,[9–11] broadband absorption,[12–14] and electromagnetically induced transparency (EIT),[15–17] which have promoted various applications such as metalens,[18–20] invisibility cloaks,[21,22] and biochemical sensors.[23–25] Benefitting from their low loss and high efficiency, metamaterial-based compact sensors show potential for signal capture and transduction applications.[26,27] For instance, quasi-bound states in the continuum (quasi-BIC) enabled by metamaterials show an ultra-high quality (Q) factor with minimum coupling to radiation channels, enabling ultrasensitive detection of biomolecules and chemical fingerprints.[28,29] However, there have been no reports on electromagnetic metamaterials for use as force-sensing elements to detect pressure or fluid flow rate, as their intrinsic optical properties are insensitive to these mechanical quantities.

The microelectromechanical system (MEMS) technology which enables the realization of three-dimensional movable structures provides an effective solution for metamaterial-based pressure sensors. By integrating with the MEMS technique, the configuration of metamaterials can undergo geometrical changes under an external force. Thus, the electromagnetic response of the metamaterial to varying pressure or fluid flow rate is achieved.[30–32] Nevertheless, existing research on MEMS-based metamaterials for pressure sensors relies on flexible substrates or dielectric layers,[33–36] which blocks the consistency of performance and limits the practical applications of these devices.

In this study, we propose a design for a TSM device and apply it as a pressure sensor by integrating it with MEMS technology. Unlike the aforementioned methods of utilizing flexible materials, reconfigurable metamaterials are designed using the MEMS technique, which enables variation in the deformation degree of spiral structures after release from the substrate. Due to the absence of flexible materials, greater compatibility with integrated circuit technology can be achieved during the fabrication process, thus achieving mass production and promoting device uniformity. To maintain the efficiency of the TSM device when detecting various pressures, this study begins with the optimization of the geometrical parameters of the spiral structures, achieving near-perfect absorption at 2.055 THz. Then, the TSM device is designed as a pressure sensor, and its electromagnetic response to different pressures is studied. The device exhibits a linear pressure sensitivity of 75 GHz kPa^{-1}.

[a]*School of Electronics and Information Technology, Sun Yat-Sen University, Guangzhou 510006, China*
[b]*Sichuan University, Chengdu, 610207, China. E-mail: yusheng.lin@scupi.cn*

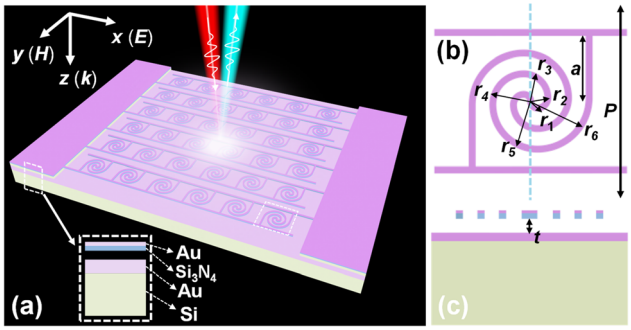

Fig. 1 Schematic drawings of the (a) 3D view of the TSM device, (b) top view, and (c) cross-sectional view of the TSM unit cell.

Additionally, the sensing performance of the TSM device to the surrounding environment is also investigated by changing the ambient refractive index from 1.0 to 1.5. Such a TSM device can be exploited for THz optoelectronic applications and provides an avenue for multifunctional THz sensors used for capturing and transducing mechanical signals and biochemical signals.

2. Designs and methods

Fig. 1 shows the schematic drawing of the proposed design of the TSM device and the construction of the unit cell. As illustrated in Fig. 1(a), the TSM device is composed of two-layer spiral-shaped arrays stacked by gold (Au) and silicon nitride (Si_3N_4) on a silicon (Si) substrate surface with a thin-film Au reflective mirror layer atop, where the air gap between the meta-atoms and Au reflective mirror layer can be varied pneumatically. Fig. 1(b) and (c) denote the geometrical parameters of TSM unit cells, including the radius (r_1 to r_6) of the quarter circles that make up the spiral, the length (a) of the cantilever, the period (P) of the unit cells, and the thickness (t) of the air gap. In this design, the radius is set as $r_1 = 7.5$ μm, $r_2 = 10$ μm, $r_3 = 20$ μm, and $r_{i+2} - r_i = 15$ μm ($i = 2, 3, 4$) to make up the spiral shape, and the linewidth of the structure constrained by ohmic dissipation effects and lithographic resolution limitations in the fabrication process is set as 5 μm, while other parameters are initially set as $a = 45$ μm, $P = 120$ μm, and $t = 2.5$ μm, respectively.

In the THz band, the permittivity of the Au material is related to the frequency and can be characterized by the Drude–Lorentz mode, which is expressed by[37,38]

$$\varepsilon_{Au}(f) = \varepsilon_\infty - \frac{{\omega_p}^2}{2\pi f(i\nu_c + 2\pi f)} \quad (1)$$

where f is the frequency of the electromagnetic wave, ε_∞ is a constant contribution to the real part of the permittivity from a high-frequency electronic transition, ω_p is the plasma frequency with a value of 1.29×10^{16} rad s^{-1}, and ν_c is a damping constant with a value of 4.12×10^{13} rad s^{-1}.[39,40] Besides, the Si_3N_4 material used in the simulation exhibits low loss, and the real and imaginary components of the permittivity are 7.6 and 0.04, respectively.[41,42]

To calculate the electromagnetic responses of the proposed TSM device and its performance in pneumatic pressure sensing applications, the finite-element simulation software COMSOL Multiphysics 6.0 is applied. The computational model integrates both solid mechanics and electromagnetic waves to simultaneously solve their coupled governing equations. In the simulations, the incident THz electromagnetic wave is set as an x-polarized plane wave at a period port, while the periodic boundary conditions are adopted in x- and y-axis directions, and the perfectly matched layer is assumed in the z-axis direction.

3. Results and discussion

To improve the efficiency and performance of the proposed TSM device used in pneumatic pressure sensing applications, the period of the TSM unit cells and the thickness of the air gap are studied to achieve perfect absorption. Fig. 2 shows the influence of the period denoted as P on the absorption spectra of the proposed TSM device. As depicted in Fig. 2(a), by increasing the P values from 120 μm to 170 μm at intervals of 10 μm, the resonant frequency is redshifted from 2.165 THz to 1.915 THz and the highest absorptivity is obtained at the period of 140 μm. The relationship between the resonances and absorption spectra of the TSM device with different P values is summarized in Fig. 2(b). It indicates that the resonances changed almost linearly along with the period and the highest absorptivity is 98.42% at 2.055 THz. The redshift of resonances

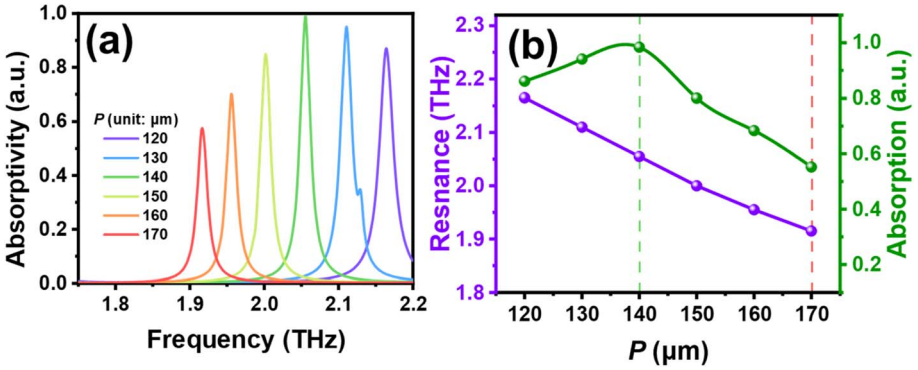

Fig. 2 (a) Absorption spectra of the TSM device with different P values. (b) Relationships between resonances, absorptivities, and P values.

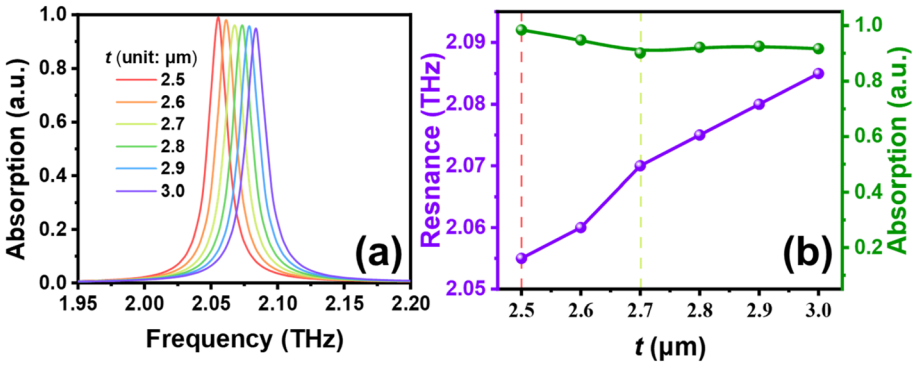

Fig. 3 (a) Absorption spectra of the TSM device with different t values. (b) Relationships between resonances, absorptivities, and t values.

when increasing periods is in accordance with the sub-wavelength response of the metamaterial. Meanwhile, the highest absorptivity achieved at the period of 140 μm can be attributed to the more concentrated localized electromagnetic energy at the resonance of the TSM device, which is also revealed by the comparison of E-field distributions at resonances for the highest and lowest absorptivity as shown in Fig. 4(a) and (b), respectively. These results also provide a design for variable optical attenuators since the optional absorptivity is attained by simply changing the geometric dimensions.

The variation of the absorption spectra of the TSM device with the thickness of the air gap is then investigated in Fig. 3. As illustrated in Fig. 3(a), with the increment of the t values from 2.5 μm to 3.0 μm, the resonances are slightly blueshifted from 2.055 THz to 2.085 THz, which trend is consistent with the lumped equivalent circuit model and the blueshift of the resonances is caused by the decrement of the capacitor formed by the spiral structures and reflective mirror layers.[43,44] Similarly, the trend of the resonances and the corresponding absorptivities at resonances with different t values of the TSM device are plotted in Fig. 3(b). The highest absorptivity of the TSM device with t values of 2.5 μm at 2.055 THz and the lowest absorptivity of the TSM device with t values of 2.7 μm at 2.070 THz are more clearly manifested. The corresponding E-field distributions are also analyzed, and the results are exhibited in Fig. 4(a) and (c), indicating the decrement in the electromagnetic energy and the attenuation of the coupling effect.

By encapsulating the TSM device in a polydimethylsiloxane (PDMS) fluidic channel, the microfluidics-based pressure sensor is implemented. As shown in Fig. 5(a) and (b), the forces acting on the TSM device are related to the fluid flow rate,[45] which causes the deformation of the spiral structures. Since the electromagnetic responses of the TSM device are highly dependent on the configuration of the unit cells, the capture and transduction of the mechanical signals are then realized.

Fig. 6 shows the performance of the microfluidics-based TSM device designed as a pneumatic pressure sensor upon applying varying pressures from 0.0 kPa to 1.4 kPa at intervals of 0.2 kPa. As shown in Fig. 6(a), with the increment of the applied pressure, the resonance of the TSM device changes from 2.055 THz to 1.800 THz. In particular, when the pressure is less than 0.8 kPa, the absorptivity remains high, more than 0.8, and the calculated linear sensitivity to pressure is 75 GHz kPa^{-1}, as plotted in Fig. 6(b). However, when the pressure exceeds 0.8 kPa, the sensitivity is no longer linear, and the absorptivity drops sharply though a much higher sensitivity is realized. Besides, the Q-factor defined by the ratio of the resonance to the full width at half maximum (FWHM) is also calculated and plotted in Fig. 6(b), which remains greater than 100. These results imply that the microfluidics-based TSM device is a competitive candidate for detecting mechanical signals and measuring fluid velocity.

Furthermore, considering the fact that the localized plasmon resonance frequency is dependent on the refractive index of surroundings and the phase shift upon plasmon excitation varies with different refractive indices,[46] the environmental

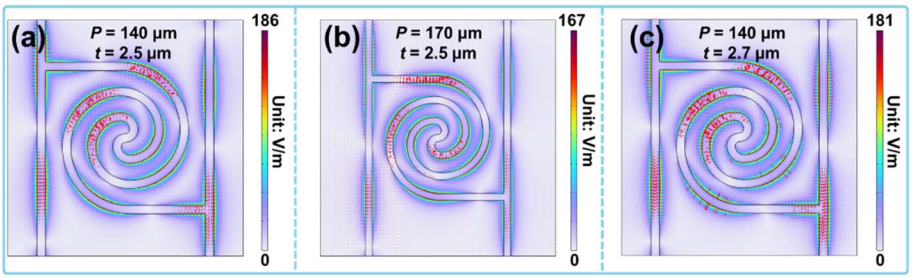

Fig. 4 Comparisons of E-field distributions at resonances of (a) 2.055 THz, (b) 1.915 THz, and (c) 2.070 THz for the highest and lowest absorptivity.

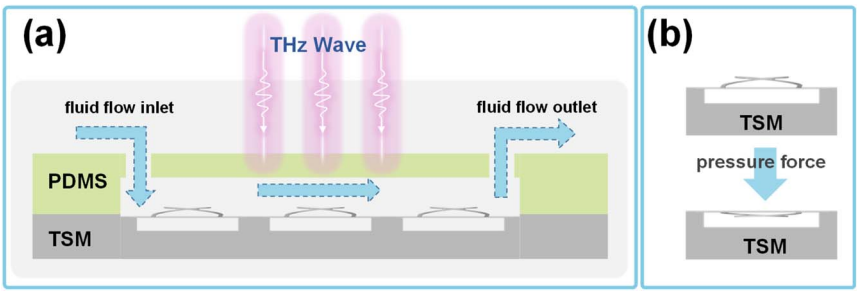

Fig. 5 (a) Schematic drawing of (a) the microfluidics-based TSM device for pneumatic pressure sensing applications. (b) Deformation states of the microfluidics-based TSM device with different pressure forces.

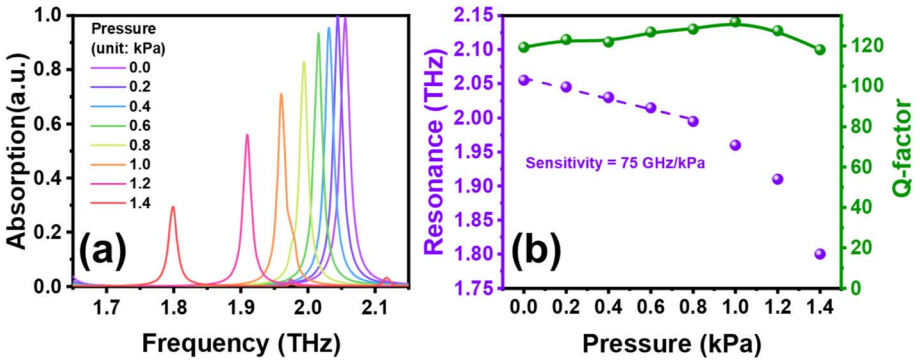

Fig. 6 (a) Absorption spectra of the microfluidics-based TSM device with different pressure forces. (b) Relationships of resonances, Q-factor, and pressure forces. The maximum sensitivity of the microfluidics-based TSM device to pressure force is 75 GHz kPa^{-1}.

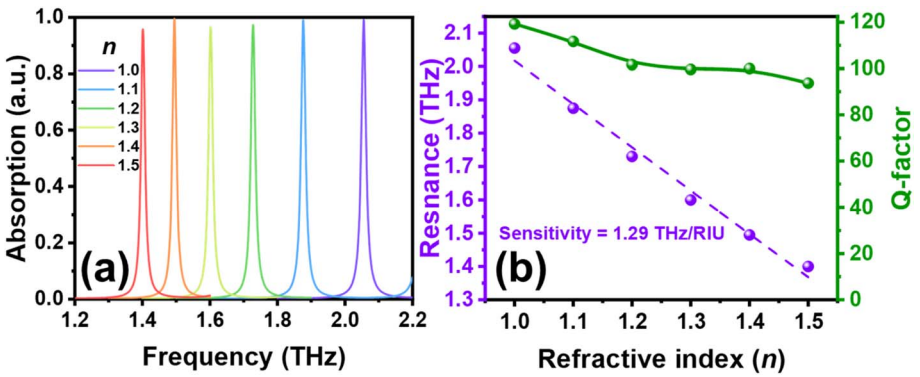

Fig. 7 (a) Absorption spectra of the MEMS-based TSM device exposed to the environment with different refractive indices. (b) Relationships of the resonances, Q-factors, and refractive indices.

sensing capability of the microfluidics-based TSM device is analyzed. By increasing the refractive index from 1.0 to 1.5, the absorption spectra of the TSM device are simulated and the results are summarized in Fig. 7. While maintaining an absorptivity greater than 0.9, the resonances are redshifted from 2.055 THz to 1.400 THz. Simultaneously, the sensitivity to surroundings defined by the spectral shift per refractive index unit (RIU) and the Q-factor are also calculated and demonstrated in Fig. 7(b), where the former is 1.29 THz/RIU and the latter remains greater than 90. The performance is superior to that of previously reported metamaterial-based sensors,[47–49] highlighting its potential in the detection of biomolecules and chemical fingerprints.

4. Conclusion

In conclusion, we have designed a MEMS-based TSM device to investigate its sensing performance in pneumatic pressure and environmental sensing applications. The geometrical parameters, specifically the period and the thickness of the air gap, are optimized by analyzing their influence on the absorption spectra of the TSM device. The near-perfect absorption is then

realized at 2.055 THz for the TSM device with the P and t values kept as 140 μm and 2.5 μm, respectively. Meanwhile, the electromagnetic responses of the TSM device are analyzed by comparing the E-field distributions at the resonance of the highest and the lowest absorptivity when varying the parameters, and the compatible localized electromagnetic energy density is revealed. Then, the pneumatic pressure sensor is characterized by applying different pressures to the TSM device, demonstrating high efficiency with a sensitivity of 75 GHz kPa^{-1}. Moreover, the relationship between the absorption spectra and the refractive indices is also investigated, revealing a sensitivity of up to 1.29 THz per RIU and a Q-factor of greater than 90. The proposed MEMS-based TSM device offers a design for THz optoelectronic devices and provides an appealing solution for compact sensors used for capturing and transducing mechanical signals or biochemical signals. Future studies will concentrate on advancing MEMS technology integration to enhance the practical implementation potential of the proposed TSM framework.

Data availability

The data that support the findings of this study are available from the corresponding author upon reasonable request.

Conflicts of interest

There are no conflicts to declare.

Acknowledgements

The authors acknowledge the financial support from the Guangdong Science and Technology Program (2024A0505050007) and Guangdong Basic and Applied Basic Research Foundation (2024A1515013019).

References

1 J. B. Pendry, D. Schurig and D. R. Smith, Controlling Electromagnetic Fields, *Science*, 2006, **312**, 1780–1782.
2 C. Sheng, H. Liu, Y. Wang, S. N. Zhu and D. A. Genov, Trapping Light by Mimicking Gravitational Lensing, *Nat. Photonics*, 2013, **7**, 902–906.
3 N. Yu, P. Genevet, M. A. Kats, F. Aieta, J.-P. Tetienne, F. Capasso and Z. Gaburro, Light Propagation with Phase Discontinuities: Generalized Laws of Reflection and Refraction, *Science*, 2011, **334**, 333–337.
4 R. A. Shelby, D. R. Smith and S. Schultz, Experimental Verification of a Negative Index of Refraction, *Science*, 2001, **292**, 77–79.
5 V. M. Shalaev, Optical Negative-Index Metamaterials, *Nat. Photonics*, 2007, **1**, 41–48.
6 J. Valentine, S. Zhang, T. Zentgraf, E. Ulin-Avila, D. A. Genov, G. Bartal and X. Zhang, Three-Dimensional Optical Metamaterial with a Negative Refractive Index, *Nature*, 2008, **455**, 376–379.
7 A. Leitis, A. Tittl, M. Liu, B. H. Lee, M. B. Gu, Y. S. Kivshar and H. Altug, Angle-Multiplexed All-Dielectric Metasurfaces for Broadband Molecular Fingerprint Retrieval, *Sci. Adv.*, 2019, **5**, eaaw2871.
8 M. S. Bin-Alam, O. Reshef, Y. Mamchur, M. Z. Alam, G. Carlow, J. Upham, B. T. Sullivan, J.-M. Ménard, M. J. Huttunen, R. W. Boyd and K. Dolgaleva, Ultra-High-Q Resonances in Plasmonic Metasurfaces, *Nat. Commun.*, 2021, **12**, 974.
9 H. Li, Q. Jia, G. Yang, A. Jiang, M. Ni, F. Cao, B. Lyu, D. Liu and J. Shi, Nonlocal Metasurface with Chiral Exceptional Points in the Telecom-Band, *Nano Lett.*, 2024, **24**, 2087–2093.
10 J. Bao, X. Chen, K. Liu, Y. Zhan, H. Li, S. Zhang, Y. Xu, Z. Tian and T. Cao, Nonvolatile Chirality Switching in Terahertz Chalcogenide Metasurfaces, *Microsyst. Nanoeng.*, 2022, **8**, 112.
11 M. V. Gorkunov, A. A. Antonov and Y. S. Kivshar, Metasurfaces with Maximum Chirality Empowered by Bound States in the Continuum, *Phys. Rev. Lett.*, 2020, **125**, 093903.
12 W. Li, S. Cheng, Z. Yi, H. Zhang, Q. Song, Z. Hao, T. Sun, P. Wu, Q. Zeng and R. Raza, Advanced Optical Reinforcement Materials Based on Three-Dimensional Four-way Weaving Structure and Metasurface Technology, *Appl. Phys. Lett.*, 2025, **126**, 033503.
13 Z. Li, S. Cheng, H. Zhang, W. Yang, Z. Yi, Y. Yi, J. Wang, S. Ahmad and R. Raza, Ultrathin Broadband Terahertz Metamaterial Based on Single-Layer Nested Patterned Graphene, *Phys. Lett. A*, 2025, **534**, 130262.
14 Z. Ai, H. Liu, S. Cheng, H. Zhang, Z. Yi, Q. Zeng, P. Wu, J. Zhang, C. Tang and Z. Hao, Four Peak and High Angle Tilted Insensitive Surface Plasmon Resonance Graphene Absorber Based on Circular Etching Square Window, *J. Phys. D: Appl. Phys.*, 2025, **58**, 185305.
15 H. Liu, C. Guo, G. Vampa, J. L. Zhang, T. Sarmiento, M. Xiao, P. H. Bucksbaum, J. Vučković, S. Fan and D. A. Reis, Enhanced High-Harmonic Generation from an All-Dielectric Metasurface, *Nat. Phys.*, 2018, **14**, 1006–1010.
16 T. Zhou, S. Chen, X. Zhang, X. Zhang, H. Hu and Y. Wang, Electromagnetically induced transparency based on a carbon nanotube film terahertz metasurface, *Opt. Express*, 2022, **30**, 15436–15445.
17 Y. Yang, I. I. Kravchenko, D. P. Briggs and J. Valentine, All-Dielectric Metasurface Analogue of Electromagnetically Induced Transparency, *Nat. Commun.*, 2014, **5**, 5753.
18 F. Aieta, P. Genevet, M. A. Kats, N. Yu, R. Blanchard, Z. Gaburro and F. Capasso, Aberration-free Ultrathin Flat Lenses and Axicons at Telecom Wavelengths Based on Plasmonic Metasurfaces, *Nano Lett.*, 2012, **12**, 4932–4936.
19 Y. Liu and Y.-S. Lin, Stretchable Dual-Axis Terahertz Bifocal Metalens with Flexibly Polarization-Dependent Focal Position and Direction, *ACS Appl. Mater. Interfaces*, 2024, **16**, 34338–34348.
20 R. Wang, M. A. Ansari, H. Ahmed, Y. Li, W. Cai, Y. Liu, S. Li, J. Liu, L. Li and X. Chen, Compact Multi-Foci Metalens Spectrometer, *Light:Sci. Appl.*, 2023, **12**, 103.

21 J. S. Choi and J. C. Howell, Paraxial Ray Optics Cloaking, *Opt. Express*, 2014, **22**, 29465–29478.
22 X. Ni, Z. J. Wong, M. Mrejen, Y. Wang and X. Zhang, An Ultrathin Invisibility Skin Cloak for Visible Light, *Science*, 2015, **349**, 1310–1314.
23 J. García-Guirado, M. Svedendahl, J. Puigdollers and R. Quidant, Enhanced Chiral Sensing with Dielectric Nanoresonators, *Nano Lett.*, 2020, **20**, 585–591.
24 D. Zheng and Y.-S. Lin, Angular-Dispersive Narrowband Absorption Induced by Quasi-BIC in SiO_2-Au Metamaterial, *Small Struct.*, 2024, **5**, 2300529.
25 S. Cheng, W. Li, H. Zhang, M. N. Akhtar, Z. Yi, Q. Zeng, C. Ma, T. Sung, P. Wu and S. Ahmad, High Sensitivity Five Band Tunable Metamaterial Absorption Device Based on Block like Dirac Semimetals, *Opt. Commun.*, 2024, **569**, 130816.
26 A. Tittl, A. Leitis, M. Liu, F. Yesilkoy, D.-Y. Choi, D. N. Neshev, Y. S. Kivshar and H. Altug, Imaging-Based Molecular Barcoding with Pixelated Dielectric Metasurfaces, *Science*, 2018, **360**, 1105–1109.
27 Z. Zeng, H. Liu, H. Zhang, S. Cheng, Y. Yi, Z. Yi, J. Wang and J. Zhang, Tunable Ultra-Sensitive Four-Band Terahertz Sensors Based on Dirac Semimetals, *Photonic. Nanostruct.*, 2025, **63**, 101347.
28 F. Yesilkoy, E. R. Arvelo, Y. Jahani, M. Liu, A. Tittl, V. Cevher, Y. Kivshar and H. Altug, Ultrasensitive Hyperspectral Imaging and Biodetection Enabled by Dielectric Metasurfaces, *Nat. Photonics*, 2019, **13**, 390–396.
29 S. Romano, G. Zito, S. Managò, G. Calafiore, E. Penzo, S. Cabrini, A. C. De Luca and V. Mocella, Surface-Enhanced Raman and Fluorescence Spectroscopy with anAll-Dielectric Metasurface, *J. Phys. Chem. C*, 2018, **122**, 19738–19745.
30 Y.-S. Lin and C. Lee, Tuning Characteristics of Mirrorlike T-shape Terahertz Metamaterial Using Out-of-Plane Actuated Cantilevers, *Appl. Phys. Lett.*, 2014, **104**, 251914.
31 F. Ding, Y. Deng, C. Meng, P. C. V. Thrane and S. I. Bozhevolnyi, Electrically Tunable Topological Phase Transition in Non-Hermitian Optical MEMS Metasurfaces, *Sci. Adv.*, 2024, **10**, eadl4661.
32 X. Zhao, J. Schalch, J. Zhang, H. R. Seren, G. Duan, R. D. Averitt and X. Zhang, Electromechanically Tunable Metasurface Transmission Waveplate at Terahertz Frequencies, *Optica*, 2018, **5**, 303–310.
33 H. Jeong, Y. Cui, M. M. Tentzeris and S. Lim, Hybrid (3D and Inkjet) Printed Electromagnetic Pressure Sensor Using Metamaterial Absorber, *Addit. Manuf.*, 2020, **35**, 102405.
34 Y. Liu, Y. Chen, J. Li, C. Zhang, Q. Wu, N. Su and M. Li, Terahertz Biaxial Strain Sensor Based on Double-Upright Cross Metamaterial, *Micromachines*, 2024, **14**, 816.
35 M. Bakır, M. Karaaslan, O. Akgol and C. Sabah, Multifunctional Metamaterial Sensor Applications Based on Chiral Nihility, *Opt. Quantum Electron.*, 2017, **49**, 346.
36 R. Melik, E. Unal, N. K. Perkgoz, C. Puttlitz and H. V. Demir, Metamaterial-Based Wireless Strain Sensors, *Appl. Phys. Lett.*, 2009, **95**, 011106.
37 M. G. Blaber, M. D. Arnold and M. J. Ford, Search for the Ideal Plasmonic Nanoshell: The Effects of Surface Scattering and Alternatives to Gold and Silver, *J. Phys. Chem. C*, 2009, **113**, 3041–3045.
38 C. A. Jones, S. F. Helfert, J. Jahns, S. Limmer and D. Fey, Wave Guiding Properties of Ribbed Surface Waveguides in Three Frequency Domains, *Opt. Quantum Electron.*, 2013, **45**, 245–255.
39 M. A. Ordal, R. J. Bell, R. W. Alexander, L. L. Long and M. R. Querry, Optical Properties of Fourteen Metals in the Infrared and Far Infrared: Al, Co, Cu, Au, Fe, Pb, Mo, Ni, Pd, Pt, Ag, Ti, V, and W, *Appl. Opt.*, 1985, **24**, 4493–4499.
40 B. Li and Y.-S. Lin, Tunable Terahertz Perfect Absorber Using Vanadium Dioxide-Based Metamaterial for Sensing Applications, *J. Alloys Compd.*, 2024, **983**, 173922.
41 H. Paik and K. D. Osborn, Reducing Quantum-Regime Dielectric Loss of Silicon Nitride for Superconducting Quantum Circuits, *Appl. Phys. Lett.*, 2010, **96**, 072505.
42 G. Cataldo, J. A. Beall, H.-M. Cho, B. McAndrew, M. D. Niemack and E. J. Wollack, Infrared Dielectric Properties of Low-Stress Silicon Nitride, *Opt. Lett.*, 2012, **37**, 4200–4202.
43 Y. Chang, J. Wei and C. Lee, Metamaterials – from Fundamentals and MEMS Tuning Mechanisms to Applications, *Nanophotonics*, 2020, **9**, 3049–3070.
44 K. Yang, X. Yao, B. Liu and B. Ren, Metallic Plasmonic Array Structures: Principles, Fabrications, Properties, and Applications, *Adv. Mater.*, 2021, **33**, 2007988.
45 M. A. Schmidt, R. T. Howe, S. D. Senturia and J. H. Haritonidis, Design and Calibration of a Microfabricated Floating-Element Shear-Stress Sensor, *IEEE Trans. Electron Devices*, 1988, **35**, 750–757.
46 R. Ameling, L. Langguth, M. Hentschel, M. Mesch, P. V. Braun and H. Giessen, Cavity-Enhanced Localized Plasmon Resonance Sensing, *Appl. Phys. Lett.*, 2010, **97**, 253116.
47 A. S. Saadeldin, M. F. O. Hameed, E. M. A. Elkaramany and S. S. A. Obayya, Highly Sensitive Terahertz Metamaterial Sensor, *IEEE Sens. J.*, 2019, **19**, 7993–7999.
48 J. Zhang, N. Mu, L. Liu, J. Xie, H. Feng, J. Yao, T. Chen and W. Zhu, Highly Sensitive Detection of Malignant Glioma Cells Using Metamaterial-Inspired THz Biosensor Based on Electromagnetically Induced Transparency, *Biosens. Bioelectron.*, 2021, **185**, 113241.
49 Z. Li, Y. Cheng, H. Luo, F. Chen and X. Li, Dual-Band Tunable Terahertz Perfect Absorber Based on All-Dielectric InSb Resonator Structure for Sensing Application, *J. Alloys Compd.*, 2022, **925**, 166617.